Shape coexistence in Ne isotopes and hyperon impurity effect on low-lying states

Huai-Tong Xue (薛怀通),[1,2] Ji-Wei Cui (崔继伟),[3] Q. B. Chen (陈启博),[2]
Xian-Rong Zhou (周先荣),[2,*] and Hiroyuki Sagawa[4]

[1]*College of Physics and Electronic Engineering, Nanyang Normal University, Nanyang 473061, China*
[2]*Department of Physics, East China Normal University, Shanghai 200241, China*
[3]*School of Physics and Optoelectronic Engineering, Xidian University, Xi'an 710071, China*
[4]*Center for Mathematical Sciences, University of Aizu Aizu-Wakamatsu, Fukushima 965-8580, Japan*

(Received 23 July 2024; accepted 20 September 2024; published 10 October 2024)

Based on the beyond-mean-field Skyrme-Hartree-Fock model, we investigate the shape coexistence in Ne isotopes and the effect of Λ hyperon on the energy level structure in the nuclei. The up-to-date Skyrme-type $N\Lambda$ interaction SLL4 and the NN interaction SGII are employed. Low-lying energy spectra of ^{20,22,24,26,28,30,32,34}Ne, including the low-lying states with $J \leqslant 6$, are predicted, discussed in detail, and found in good agreement with experimental results. The electric quadrupole transition rates are also examined. The coexistences of a ground state rotational band and a β vibrational band are revealed in ^{20,22,24}Ne. Unlike the previously discovered shrinkage effect of Λ_s on the ground state nuclei, it is found that the Λ_s may alter the excitation mode of the second band by affecting the distribution of the collective wave function, thereby causing the β vibrational band transitions to a vibrational band with equidistant energy levels.

DOI: 10.1103/PhysRevC.110.044310

I. INTRODUCTION

The shape of a nucleus is one of its most fundamental properties, and its exploration across the nuclear landscape provides insight into the mechanisms underlying how protons and neutrons are organized [1]. Nuclear shape coexistence is the phenomenon in which distinct shapes occur within the same nucleus and at a similar energy. Minima in the total nuclear potential energy can be found for shapes that include spherical, axially symmetric prolate or oblate deformed ellipsoids, axially nonsymmetric (triaxial) ellipsoids, etc. [2]. The lowest minimum is associated with the mass and shape of the nucleus.

After it was first proposed in 1956, shape coexistence has been observed in heavy and medium-heavy nuclei, as well as light nuclei thanks to many experimental [3] and theoretical attempts [4,5]. For example, shape coexistence has been observed in nuclei with $Z \approx 82$ [6], $Z \approx 50$ [7], $Z \approx 40$, and $N \approx 60$ [8–10], $Z \approx 64$, and $N \approx 90$ [11], $Z \approx 34$ and $N \approx 40$ [12], nuclei in the light mass region with $N = Z$, and nuclei in the island of inversion with $(N, Z) = (8, 6)$, $(20, 12)$, and $(28, 14)$. In recent years, an up-to-date view of the experimental manifestation of shape coexistence in nuclei and theories predicting its occurrence think that there appears to be a possibility that it occurs in all nuclei [4].

At the same time, various theoretical approaches were developed to describe nuclear shape coexistence, including the interacting shell model [13], the Monte Carlo shell model [14], the interacting boson model [15], and both nonrelativistic [16,17] and relativistic/covariant [18] density functional theories (DFTs).

Among these approaches, nuclear DFT stands out as the most efficient microscopic method capable of offering a unified and consistent description for a wide range of nuclei across the nuclear chart [16]. Initially designed as a ground-state theory, nuclear DFT necessitates expansion beyond the mean-field level to address nuclear spectroscopic properties adequately. One viable solution involves the utilization of a beyond-mean-field approach, which encompasses angular momentum projection (AMP) techniques and the generator coordinate method (GCM). Therefore, the states with different angular momenta can be projected out from the mean-field wave functions, which are calculated by DFT, such as Skyrme-Hartree-Fock (SHF), using AMP techniques. Finally, the configuration mixing of different nuclear cores is achieved through the GCM method.

The shape coexistence represents various quantum configurations with distinct spatial arrangements, all varying for the lowest energy state. This phenomenon provides an excellent platform for studying the interactions among these configurations within a single nucleus. Recently, Ne isotopes have attracted increasing interests. Thus, they have been extensively studied experimentally and theoretically. Simultaneously, some of the shape evolution and shape coexistence in Ne isotopes have been examined in multiple investigations. In Ref. [19], the isospin dependence of the shapes in Ne isotopes have been studied by analyzing the quadrupole moments and electric quadrupole transitions $B(E2)$ utilizing the deformed SHF model. As reported in Ref. [20], the quadruple deformations in Ne isotopes and the corresponding Λ hypernuclei were investigated by the deformed SHF+Bardeen-Cooper-

*Contact author: xrzhou@phy.ecnu.edu.cn

Schrieffer (BCS) model including different tensor and pairing forces. The AMP-GCM based on the Gogny force (D1S) mean field was also applied to investigate the quadrupole collectivity in neutron-rich Ne isotopes by analyzing potential energy surface (PESs) and the spectroscopic quadrupole moments [21]. A very strong shape coexistence, which exhibited an oblate ground state and a prolate state with an energy difference of 77 keV, was predicted in ^{24}Ne. In general, numerous studies have already examined the low-lying states of even-even neon isotopes at the beyond mean-field level, including not only quadrupole deformation but also octupole deformation [22–30].

Meanwhile, the investigation of hypernuclei is also another hot topic in nuclear physics nowadays. The explorations of hypernuclear systems comprising nucleons and hyperons can exert far-reaching implications on nuclear physics [31,32]. In recent years, nuclear mean-field (MF) energy-density functionals (EDFs) [33–39] and beyond-MF approaches [40–44] were extended to hypernuclei.

The Λ hypernucleus, composed of an ordinary nuclear core and the lightest hyperon, provides a unique laboratory to study the ΛN interactions. In addition, Λ hyperon can induce multiple interesting effects such as the shrinkage of the nuclear size and the stabilization of the binding energies [45,46], the changes in the nuclear cluster structures [47–49], the extension of the neutron drip line [50–52], the appearance of nucleon and hyperon skin or halo [34,53]. Especially in recent years, interplay between the octupole-deformed ^{20}Ne state and a Λ hyperon has been presented in Refs. [43,54]. Although the impurity effect of hyperons on shape coexistence has been studied with the mean field aspect [55], the change of energy spectra due to the interplay between the shape coexistence and the Λ hyperon has not been carefully explored. Such researches need the restoration of rotational symmetry and interaction between different shapes, which has been successfully realized in our recent work [44].

The purpose of this paper is to use the beyond SHF model with AMP and GCM calculations to study the neon hyperisotopes from $A = 20$ up to $A = 34$ and to investigate the impurity effect of Λ hyperon on shape coexistence.

This paper is organized as follows. Section II reviews briefly the formalism of the beyond-SHF model. Section III presents the results and discussions and in Sec. IV we summarize the work.

II. THEORETICAL FRAMEWORK

The hypernuclear MF wave function obtained from a SHF calculation with a quadrupole constraint is given by

$$|\Phi^{(N\Lambda)}(\beta)\rangle = |\Phi^{N}(\beta)\rangle \otimes |\Phi^{\Lambda}\rangle \,, \tag{1}$$

where $|\Phi^{N}(\beta)\rangle$ and $|\Phi^{\Lambda}\rangle$ are intrinsic wave functions of the nuclear core and of the Λ hyperon, respectively. More specifically, the hyperon wave function for single-Λ hypernuclei is

$$|\Phi^{\Lambda}\rangle = \varphi_s(\Lambda) \tag{2}$$

and

$$|\Phi^{N}(\beta)\rangle = \prod_{k>0}(u_k + v_k a_k^{+} a_{\bar{k}}^{+})|\mathrm{HF}\rangle \tag{3}$$

is a BCS state obtained from the nuclear SHF+BCS calculation with density-dependent δ interaction (DDDI) [56], constrained to an axially deformed shape given by the deformation parameter β, which is proportional to the quadrupole moment,

$$\beta = \frac{4\pi}{3A_c R_c^2}\langle\Phi^{N}(\beta)|r^2 Y_{20}|\Phi^{N}(\beta)\rangle \,, \tag{4}$$

where A_c is the mass number of the core nucleus, and $R_c \equiv 1.2A_c^{1/3}$ fm.

In the GCM, the hypernuclear states are given by a superposition of projected MF wave functions onto exact angular momentum J:

$$\left|\Psi_\alpha^{JM}\right\rangle = \sum_{\beta} F_\alpha^{J}(\beta)\hat{P}_{MK}^{J}|\Phi^{(N\Lambda)}(\beta)\rangle \,, \tag{5}$$

where $F_\alpha^J(\beta)$ is a weight function, and $\hat{P}_{MK}^J$ is the AMP operator, with $K = K_{\mathrm{core}} + K_\Lambda$ representing the projection of angular momentum J^π onto the intrinsic z axis.

To obtain the eigenstate $|\Psi_\alpha^{JM}\rangle$, each weight $F_\alpha^J(\beta)$ in Eq. (5) is determined by the Hill-Wheeler-Griffin (HWG) equation [57],

$$\sum_{\beta'}\left[H_{KK}^{\prime J}(\beta,\beta') - E_\alpha^J N_{KK}^J(\beta,\beta')\right]F_\alpha^J(\beta') = 0 \,, \tag{6}$$

in which the corrected Hamiltonian and norm elements are given by

$$H_{KK'}^{\prime J}(\beta,\beta') = \langle\Phi^{(N\Lambda)}(\beta')|\hat{H}'\hat{P}_{KK'}^{J}|\Phi^{(N\Lambda)}(\beta)\rangle \,, \tag{7}$$

$$N_{KK'}^{J}(\beta,\beta') = \langle\Phi^{(N\Lambda)}(\beta')|\hat{P}_{KK'}^{J}|\Phi^{(N\Lambda)}(\beta)\rangle \,. \tag{8}$$

The corrected Hamiltonian $\hat{H}'$ is defined as

$$\hat{H}' = \hat{H} - \lambda_p(\hat{N}_p - Z) - \lambda_n(\hat{N}_n - N) \,, \tag{9}$$

where the Hamiltonian $\hat{H}$ is determined by the hypernuclear EDF, and the last two terms account for the fact that the projected wave function does not provide the correct number of particles on average [58]. The projected energy curve onto a specific angular momentum is derived as

$$E_{JK}(\beta) = \frac{H_{KK}^{\prime J}(\beta,\beta)}{N_{KK}^{J}(\beta,\beta)} \,. \tag{10}$$

Since the projected states do not form an orthogonal basis, $F_\alpha^J(\beta)$ are nonorthogonal functions [42], and orthogonal collective wave functions are constructed as

$$g_\alpha^J(\beta) = \sum_{\beta'}\left[\mathscr{R}^{\frac{1}{2}}\right]^{J}(\beta,\beta')F_\alpha^J(\beta') \,, \tag{11}$$

which are weights of the natural states in the collective subspace [57]. In addition,

$$\left[\mathscr{R}^{\frac{1}{2}}\right]^{J}(\beta,\beta') = \sum_k \sqrt{n_k}\, w_k(\beta) w_k^*(\beta'), \tag{12}$$

with the eigenfunctions w_k and eigenvalues n_k of the norm operator, Eq. (8), in the projected space. The average deformation

$$\bar{\beta}_\alpha^J = \sum_\beta \left|g_\alpha^J(\beta)\right|^2 \beta \tag{13}$$

TABLE I. Ground-state deformations obtained from different calculations compared with the observed ones. Among them, $\beta_{\rm MF}$ and $\beta_{\rm AMP}$ indicate the minima of the mean-field PES and AMP PES, respectively. $\bar{\beta}$ [Eq. (13)], $\overline{|\beta|}$ [Eq. (14)] are the average deformation of the ground state (0^+) given by configuration mixing of this current paper. It can indicate the signal of shape coexistence by comparing $\bar{\beta}$ [Eq. (13)] with $\overline{|\beta|}$ [Eq. (14)]. $\bar{\beta}_{\rm AMD}$ is the average deformation of the ground state calculated by antisymmetric molecular dynamics, taken from Ref. [61]. Because the experimental deformation are deduced from $B(E2)$ values, the sign of deformation is not known, so the absolute value $|\beta_{\rm exp.}|$ [62] are adopted here.

	$\lvert\beta_{\rm exp.}\rvert$ [62]	$\beta_{\rm MF}$	$\beta_{\rm AMP}$	$\bar{\beta}$	$\overline{\lvert\beta\rvert}$	$\bar{\beta}_{\rm AMD}$ [61]	$\beta_{\rm HFB}$ [63,64]
^{18}Ne	0.68	0.0	0.36	0.10	0.31	–	0.0
^{20}Ne	0.72	0.53	0.59	0.52	0.63	0.46	0.50
^{22}Ne	0.57	0.51	0.62	0.50	0.59	0.39	0.50
^{24}Ne	0.41	−0.22	−0.35	−0.03	0.36	−0.25	0.25
^{26}Ne	0.39	0.16	0.29	0.09	0.27	0.22	0.00
^{28}Ne	0.36	0.16	0.29	−0.02	0.26	−0.28	0.00
^{30}Ne	0.49	0.0	0.16	0.44	0.48	0.39	0.00
^{32}Ne	–	0.35	0.35	0.31	0.39	0.33	0.40
^{34}Ne	–	0.42	0.48	−0.29	0.46	–	–

reflects the shape of the dominant configurations in the ground or excited state and indicates the band structure [59].

To avoid the cancellation of two dominant configurations with different shapes (oblate/prolate), another average deformation is introduced in this paper as

$$\overline{|\beta^J_\alpha|} = \sum_\beta |g^J_\alpha(\beta)|^2 |\beta|. \tag{14}$$

Given the weight function $F^J_\alpha(\beta)$, the root-mean-square (rms) radius is defined as

$$R^{J\alpha}_{\rm rms} = \sqrt{\sum_{\beta\beta'} F^J_\alpha(\beta')^* F^J_\alpha(\beta) \langle \Phi^{(N\Lambda)}(\beta')|r^2 \hat{P}^J_{KK}|\Phi^{(N\Lambda)}(\beta)\rangle} \tag{15}$$

with $r^2 = \frac{1}{A}\sum_k r_k^2$, and the reduced $E2$ transition rate is derived as

$$B(E2, J^+_\alpha \to J'^+_{\alpha'}) = \frac{1}{2J+1} |\langle J'^+_{\alpha'}||\hat{Q}_2||J^+_\alpha\rangle|^2 , \tag{16}$$

where the reduced matrix element is

$$\langle J'^+_{\alpha'}||\hat{Q}_2||J^+_\alpha\rangle = \sqrt{2J'+1} \sum_{M\mu\beta\beta'} F^{J'}_{\alpha'}(\beta')^* F^J_\alpha(\beta)\, C^{J'K'}_{JM2\mu} \times \langle \Phi^{(N\Lambda)}(\beta')|\hat{Q}_{2\mu}\hat{P}^J_{MK}|\Phi^{(N\Lambda)}(\beta)\rangle , \tag{17}$$

in which $C^{J'K'}_{JM2\mu}$ denotes the Clebsh-Gordon coefficients, and $\hat{Q}_{2\mu} = \sum_k e_k r_k^2 Y_{2\mu}(\varphi_k, \theta_k)$ is the electric quadrupole transition operator [60], where e_k is the charge of the kth nucleon and r_k is its position relative to the center of mass of the nucleus. Bare charges are used in this calculation (i.e., $e_p = e$ and $e_n = e_\Lambda = 0$).

III. RESULTS AND DISCUSSION

We first focus on the Ne isotopes in the mean-field aspect, and then the AMP effect on shape coexistence and the low-lying spectrum for Ne isotopes are discussed. This enables us to study the possibility of shape coexistence at different levels. We will return to the more prospective case of Ne hyperisotopes at the end.

A. Shape coexistence in Ne isotopes

Table I shows quadrupole deformations of the Ne isotopes in this current work, compared to the ones from experiments and the ones given by other models [AMD and Hartrr-Fock-Bogoliubov (HFB)]. It can be seen that, except for ^{24}Ne, ^{26}Ne, and ^{28}Ne, the deformation obtained in this work, especially the average deformation $\bar{\beta}$ of the ground state, is reasonably consistent with the experimental one, which is closer to the experimental value than that calculated by AMD. In addition, the $\overline{|\beta|}$ in Eq. (14) matches the $|\beta_{\rm exp.}|$ better than $\bar{\beta}$ in Eq. (13), especially for ^{24,26,28}Ne. For example, the $\bar{\beta}$ of ^{24}Ne is −0.03, while the $\overline{|\beta|}$ is 0.36, which is closer to 0.41. Because the deformation of the two dominant configurations is close but with opposite signs, the degree of deformation is canceled out and not truthfully reflected in $\bar{\beta}$ in this nucleus, which is also reflected in the collective wave functions. As shown in Fig. 3, one can see a strong cancellation between prolate and oblate contributions. This will be discussed in detail later. It fully demonstrates that the results of this work are reliable to a certain extent.

The mean field PESs (black solid line) are shown in Fig. 1. While the PES of ^{18}Ne has a spherical minimum, both ^{20}Ne and ^{22}Ne are prolate deformed in their ground states. In ^{20}Ne, the prolate ground state corresponds to $\beta = 0.53$, and an oblate local minimum also appears at $\beta = -0.16$ with an excitation energy of 2.71 MeV. In the case of ^{22}Ne, the ground state corresponds to $\beta = 0.51$, and another local minimum is found at $\beta = -0.24$ with an excitation energy of 3.54 MeV. The nucleus ^{24}Ne is a clear example of very strong shape coexistence in the considered isotopic chain since, while the oblate ground state is located at $\beta = -0.22$, a prolate local minimum is also found at $\beta = 0.22$ with an excitation energy with respect to the oblate ground state of 300 keV, which roughly agrees with the 77 keV obtained by Gogny mean field [21].

On the other hand, the nuclei ^{26,30}Ne show spherical ground states indicating that the $N = 16$ subshell closure [65] and $N = 20$ shell closure are preserved at the mean-field level. The mean-field PES (MFPES) of both ^{26}Ne and ^{30}Ne are

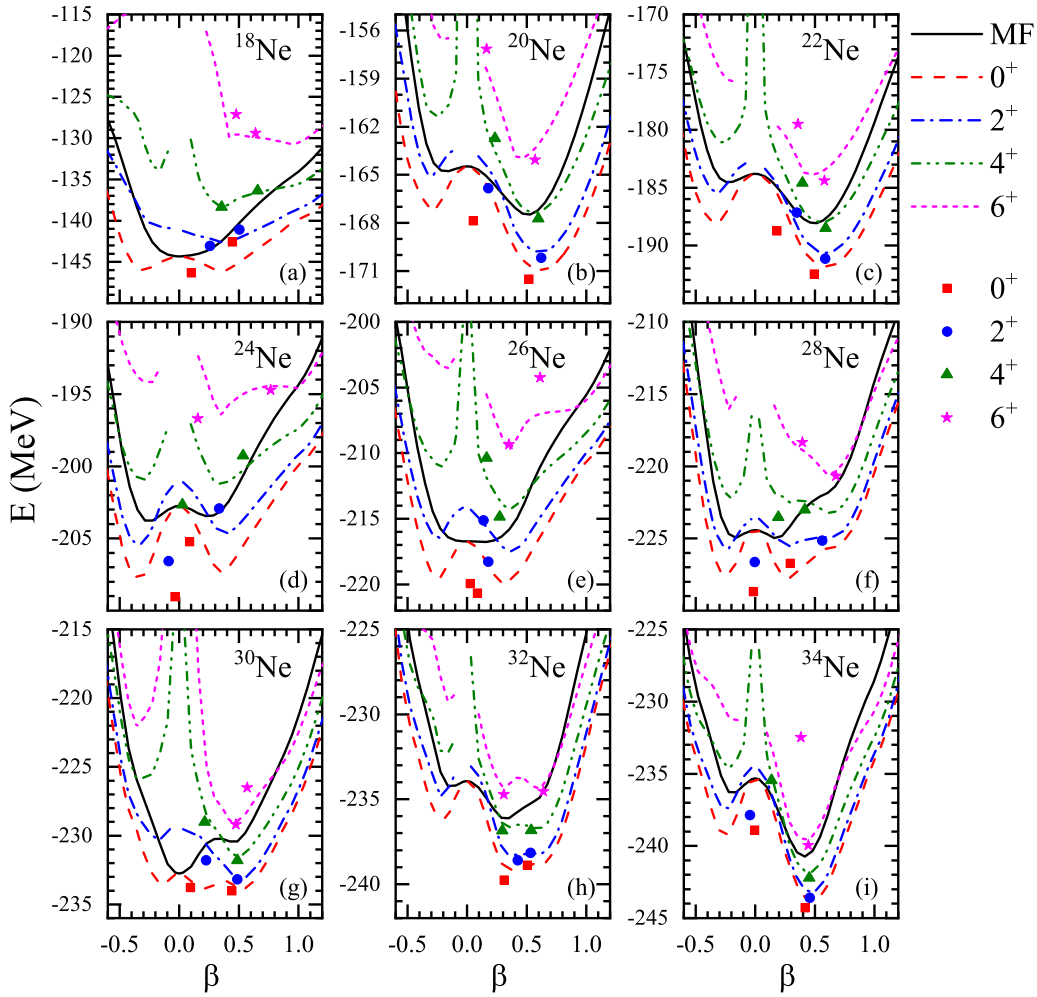

FIG. 1. Projected PESs, $E(\beta, J)$, and the GCM energy levels of Ne isotopes. The angular momentum and parity for each projected PES are given in the legend, and the mean-field PES labeled by MF is also shown for comparison. The solid bullets indicate the GCM energy levels, which are plotted at their average deformation.

particularly flat around their spherical ground states. In the case of ^{28}Ne, the ground state corresponds to $\beta = 0.16$, and another local minimum is found at $\beta = -0.16$ with an excitation energy of 30 keV higher than the ground state, indicating the existence of shape coexistence in this nucleus as well. In the nucleus ^{30}Ne we obtain a prolate shoulder at $\beta = 0.42$ at an excitation energy of 2.32 MeV with respect to the spherical ground state. In the drip line systems ^{32}Ne and ^{34}Ne, prolate deformed ground states are found. The ground states have $\beta = 0.35$ and $\beta = 0.42$, respectively. In addition, an oblate local minimum is found in ^{32}Ne/^{34}Ne at $\beta = 0.16/0.12$ with an excitation energy of 1.89/2.39 MeV with respect to the prolate ground state.

Before considering the full AMP-GCM, it is instructive to look into the angular momentum projected potential energy surfaces (AMPPES) defined as Eq. (10). The corresponding MF and AMP energy landscapes are also included for comparison. For details on the missing points in the $J = 2, 4$, and 6 curves refer to [66]. The most remarkable fact about Fig. 1 is how strongly the restoration of the rotational symmetry modifies the mean-field picture of the $J = 0$ configurations. For most isotopes, the energy barrier between the two minima is enhanced due to the restoration of rotational symmetry.

The prolate minimum is, with the exception of ^{24}Ne, the absolute minimum in all the isotopes considered, which is consistent with Gogny results [21]. The orbital responsible for such an oblate minimum is the neutron $1d_{5/2}$ orbital which becomes fully occupied in ^{24}Ne and favors oblate deformations. With increasing spin values either the energy difference between the prolate and oblate minima increases or the oblate minimum is washed out. In addition, shape coexistence is expected in the nuclei ^{24}Ne, ^{26}Ne, ^{28}Ne, and ^{30}Ne as their $J^\pi = 0^+$ prolate and oblate minima are very close in energy (446, 384, 303, and 368 keV, respectively). These minima are separated by barriers which are 5.0, 3.1, 3.3, and 1.1 MeV high, respectively.

The AMPPESs show the phenomenon of shape coexistence for some nuclei and/or some spin values, and therefore configuration mixing has to be considered in order to gain a better understanding of the structure of these states. In Fig. 1, the lowest GCM energy levels for $J = 0$ up to 6 are given. The collective levels are plotted at the average deformation deformation $\bar{\beta}$ of the mean-field states from which they are

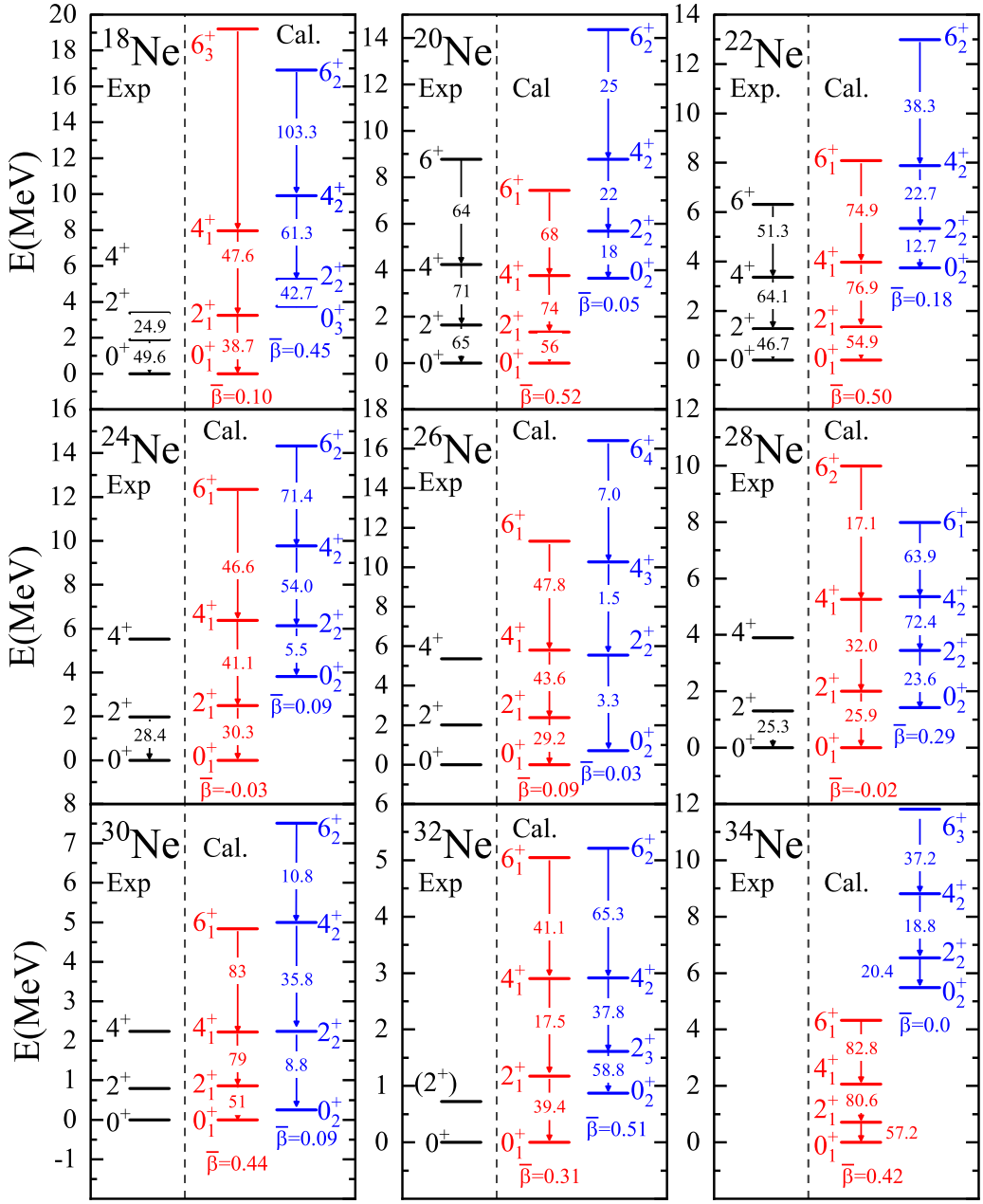

FIG. 2. The spectrum of collective states for Ne isotopes observed in the experiment (first column) and obtained from our calculation for g.s. band (second column) and another band (third column).

constructed, defined as in Eq. (13), which provides in many cases an intuitive picture of the band structure in a nucleus.

The prominent feature is that configuration mixing decreases the average deformation $\bar{\beta}$ of the ground states with respect to the minimum of the AMPPES. The ground states of the nuclei ^{24}Ne, ^{26}Ne, and ^{28}Ne become spherical, because the prolate and oblate minimum are canceled out. The other nuclei remain well deformed in their ground states and develop a rather well-defined rotational band up to the maximum spin considered for $\alpha = 1$. In addition, a well-defined rotational band is obtained for $J \geqslant 2$ in ^{20}Ne, ^{22}Ne, and ^{24}Ne. On the other hand, the excited states ($\alpha = 2$) only show a rotational band pattern for those nuclei well deformed in their ground state.

In order to provide a more detailed description of the rotational band mentioned above, we present a comparison between the ground-state excitation energy of the rotational band (almost all the ground state bands of Ne isotopes are composed of states with $\alpha = 1$, except for ^{28}Ne) and the experimental values in Fig. 2, In the same figure, the theoretical excitation energies and the values of $B(E2)$ for the possible second band are also given.

Based on the comparison of the energy of each excited state and $B(E2)$ values between them in the ground state band

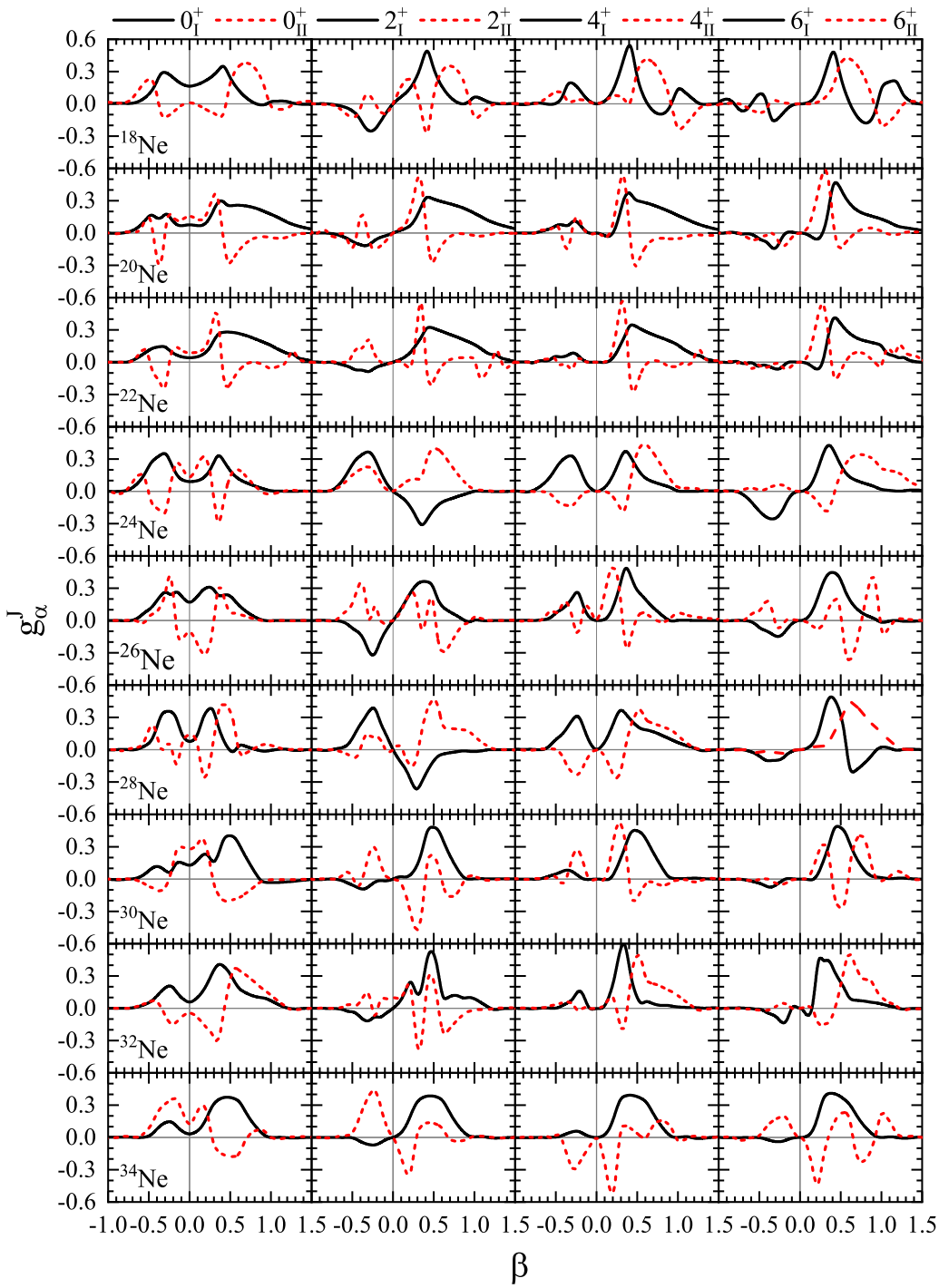

FIG. 3. Collective wave functions g^J_α for the low-lying states with $J = 0, 2, 4$, and 6 for $^{18-34}$Ne as a function of the deformation of the mean-field states from which they are constructed. Here, $g^J_{\rm I}$, $g^J_{\rm II}$ represent the wave functions of states that form the first and second band, respectively.

shown in Fig. 2 with the experimental values, it can be said that our calculation reasonably provides a rotational band that is consistent with the experimental values for every Ne isotope except for ^{18}Ne. In addition, the excitation energy levels and predicted $B(E2)$ values in the second band of these nuclei are also given in Fig. 2.

However, unlike the structure of the first band that is clearly related to rotation, the second band exhibits structural characteristics of vibration bands, some of which are more like β-vibration bands, which we will discuss in detail later in conjunction with wave functions. For $^{20-24,34}$Ne, the gap between the energy level in the band established based on the second 0^+ is roughly close to that of the ground state band. The wave function of these states of the second band in the nuclei exhibit positive and negative phase oscillations as shown in Fig. 3. The average deformation $\bar{\beta}$ of the states in the

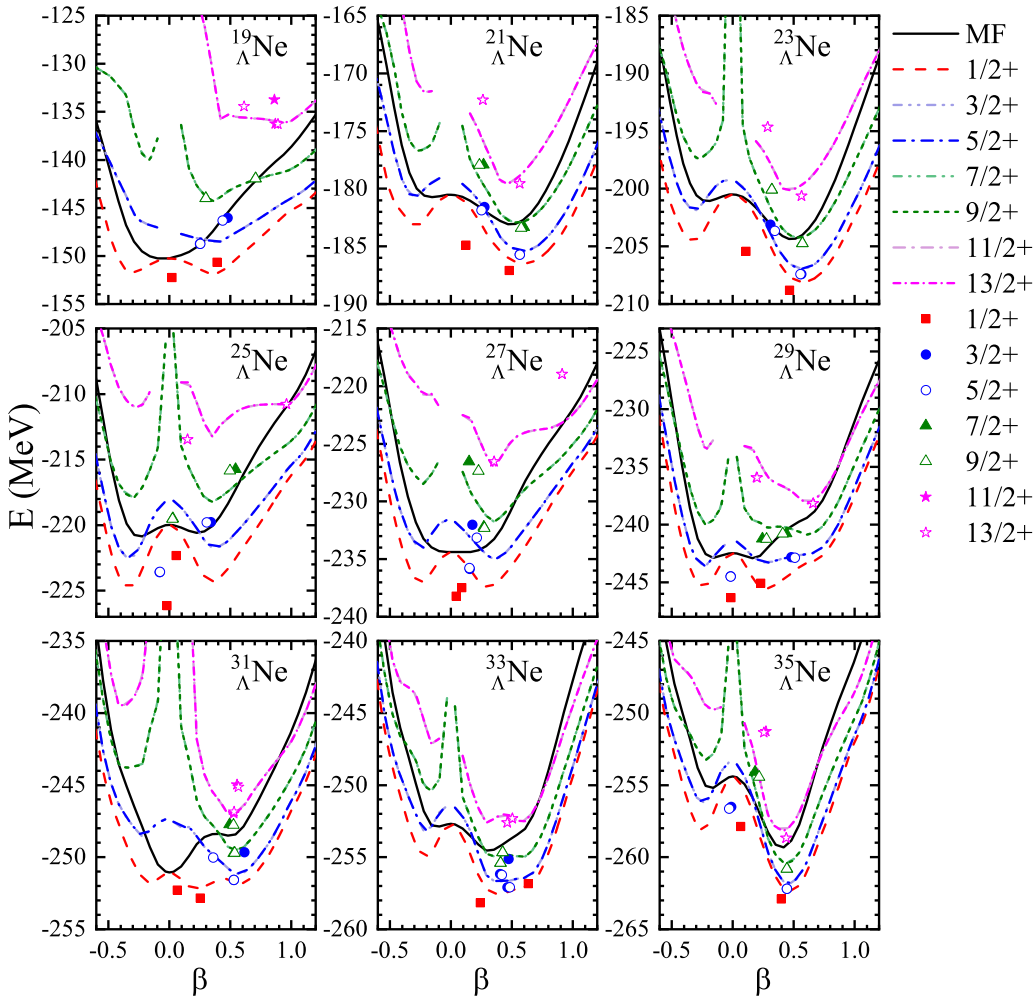

FIG. 4. Collective wave functions g^J_α for the low-lying states with $J = 1/2$-$13/2$ for Ne isotopes as a function of the deformation of the mean-field states from which they are constructed.

second band increases with the increase of angular momentum J, which reflects the fluctuations of the excited states on the shape parameter β and also reflects the increasingly important contribution of the prolate configuration. Given this, it is highly likely a β vibration band caused by collective shape fluctuations.

For the second band of ^{28,30}Ne, the spacing of energy levels within the band are roughly equal, exhibiting characteristics of vibrational bands (harmonic like spectrum [57]). As is well known, the vibrational band is generated based on spherical nucleus. Since the $\bar{\beta}$ of the states with $J \leqslant 4$ in the second band of ^{30}Ne are close to 0, it can be considered that the part of second band is a vibrational band. On the other hand, the first and second bands of ^{32}Ne are more like rotational bands built on different cores because the energy levels within each band have the characteristics of rotational bands and the average deformation of each state within a band is roughly equal.

Figure 3, however, illustrates the limits of the meaning of $\bar{\beta}$, showing the collective wave functions of the states with $J = 0, 2, 4$, and 6. All low-lying states, i.e., $0^+, 2^+, 4^+$, and 6^+ of the ground band result from mixing between prolate and oblate reference states. Especially for nuclei with spherical or weakly deformed ground states, such as ^{18,24,26,28,30}Ne, their ground states exhibit a strong mixing of prolate and oblate reference states, which leads to spherical ground states on average. However, as the angular momentum J increases, the contribution of prolate reference states increases. For nuclei with well-deformed ground states, the dominance of prolate deformations is evident. Returning to Fig. 1, the values of $\bar{\beta}$ for the states in the ground band reflect this dominance. For example, in ^{20}Ne, the $\bar{\beta}$ of each state in the ground state band (0^+_1, 2^+_1, 4^+_1, 6^+_1) is approximately equal to 0.5, which is consistent with the β of the energy minimum on the prolate side of their projected energy curves.

For states in the second band, the situation is similar to that of the ground band. The very small value of $\bar{\beta}$ does not mean that this state is nearly spherical, but rather, that the weights of prolate and oblate shapes are nearly equal. For higher J values, the mixing between oblate and prolate configurations are less pronounced as shown in Fig. 3, and the value of $\bar{\beta}$ better represents the structure of the states. For example, in ^{20}Ne, $\bar{\beta}$ of the 2^+_2, 4^+_2, and 6^+_2 excited states shown in Fig. 1 corresponds very well to the deformation values of the main components of these states shown in Fig. 3, approximately 0.3.

TABLE II. Transition rates $B(E2)$, Eq. (16), (in units of $e^2\text{fm}^4$) and the ratios Γ_B, Eq. (18).

	$^{19}_{\Lambda}$Ne		$^{21}_{\Lambda}$Ne		$^{23}_{\Lambda}$Ne		$^{25}_{\Lambda}$Ne		$^{27}_{\Lambda}$Ne		$^{29}_{\Lambda}$Ne		$^{31}_{\Lambda}$Ne		$^{33}_{\Lambda}$Ne		$^{35}_{\Lambda}$Ne	
$J_i \to J_f$	$B(E2)$	Γ_B	$B(E2)$	$\boldsymbol{\Gamma_B}$	$B(E2)$	$\boldsymbol{\Gamma_B}$	$B(E2)$	$\boldsymbol{\Gamma_B}$	$B(E2)$	Γ_B	$B(E2)$	Γ_B	$B(E2)$	Γ_B	$B(E2)$	Γ_B	$B(E2)$	$\boldsymbol{\Gamma_B}$
$3/2^+_{\text{I}} \to 1/2^+_{\text{I}}$	34.1	0.88	51.2	**0.92**	51.5	**0.94**	29.9	**0.99**	24.4	0.84	20.2	0.78	32.3	0.63	37.6	0.95	54.3	0.95
$5/2^+_{\text{I}} \to 1/2^+_{\text{I}}$	33.8	0.87	51.3	**0.92**	51.6	**0.94**	29.8	**0.98**	26.9	0.92	20.2	0.78	33.8	0.66	36.2	0.92	54.4	0.95
$7/2^+_{\text{I}} \to 3/2^+_{\text{I}}$	49.2	1.03	62.7	**0.85**	64.8	**0.84**	36.0	**0.88**	40.6	0.93	28.2	0.88	68.4	0.87	63.4	3.62	69.1	0.86
$9/2^+_{\text{I}} \to 5/2^+_{\text{I}}$	54.3	1.14	67.7	**0.91**	71.7	**0.93**	40.2	**0.98**	43.6	1.0	29.5	0.92	76.6	0.97	70.2	4.01	76.8	0.95
$11/2^+_{\text{I}} \to 7/2^+_{\text{I}}$	11.3	0.17	65.6	**0.96**	68.0	**0.91**	43.6	**0.94**	48.3	1.01	26.2	1.53	65.7	0.79	57.3	1.39	76.4	0.92
$13/2^+_{\text{I}} \to 9/2^+_{\text{I}}$	24.5	0.37	66.3	**0.98**	70.6	**0.94**	45.4	**0.97**	47.1	0.99	24.8	1.45	53.6	0.65	59.6	1.45	79.2	0.96
$J_i \to J_f$	$B(E2)$	Γ_B	$B(E2)$	Γ_B	$B(E2)$	Γ_B	$B(E2)$	Γ_B	$B(E2)$	Γ_B	$B(E2)$	Γ_B	$B(E2)$	Γ_B	$B(E2)$	Γ_B	$B(E2)$	Γ_B
$3/2^+_{\text{II}} \to 1/2^+_{\text{II}}$	42.4	0.99	18.7	1.04	8.60	0.68	5.6	1.02	2.1	0.36	15.5	0.66	5.6	0.64	24.1	0.41	22.4	1.10
$5/2^+_{\text{II}} \to 1/2^+_{\text{II}}$	46.9	1.10	18.9	1.05	8.90	0.70	4.7	0.85	11.6	3.5	16.4	0.69	2.7	0.31	12.1	0.21	21.6	1.06
$7/2^+_{\text{II}} \to 3/2^+_{\text{II}}$	47.8	0.78	21.9	0.99	12.2	0.54	47.0	0.87	0.09	0.06	48.9	0.67	67.9	1.90	0.30	0.01	30.2	1.61
$9/2^+_{\text{II}} \to 5/2^+_{\text{II}}$	46.0	0.75	25.2	1.15	27.8	1.22	55.5	1.03	28.1	18.7	51.8	0.71	64.5	1.80	1.6	0.04	31.7	1.69
$11/2^+_{\text{II}} \to 7/2^+_{\text{II}}$	7.20	0.07	24.4	0.98	3.30	0.09	31.3	0.44	0.4	0.06	71.0	1.11	66.2	6.13	60.0	0.92	48.4	1.30
$13/2^+_{\text{II}} \to 9/2^+_{\text{II}}$	5.10	0.05	34.9	1.40	3.40	0.09	30.0	0.42	0.7	0.1	67.7	1.06	58.0	5.37	62.3	0.95	49.8	1.34

B. Impurity effects of Λ_s on low-lying states in Ne isotopes

Next, let us focus on the influence of an s-state Λ hyperon on the structure of low-lying states in nuclei. First, by comparing the Fig. 1, in which the MFPES and AMPPES, as well as the low-lying states with their average deformation $\bar{\beta}$ are included, with Fig. 4, it can be seen that the influence of s-state Λ on the structure of low-lying states of the first band is not so significant, except for $^{31,33}_{\Lambda}$Ne. This is due to the fact that the s-orbit Λ is spherically distributed (or mildly deformed) and thus does not change the shape of the nuclear core dramatically. This is also demonstrated in Fig. 6, $^{21}_{\Lambda}$Ne for example, by the weights of the natural states in the collective subspace, Eq. (11). Again the weights of the $1/2^+_1(3/2^+_1$ and $5/2^+_1$, $7/2^+_1$ and $9/2^+_1$, $11/2^+_1$ and $13/2^+_1)$ states are similar to those of the corresponding $0^+_1(2^+_1$, 4^+_1, $6^+_1)$ states. However, the addition of s-state Λ has caused significant changes to many low-lying states, especially for $^{31,33}_{\Lambda}$Ne, where the band that has a rotational-like structure in their two core nuclei has been disrupted. This is somewhat different from the shrinkage effect of Λ on the ground state [44,67].

In Table II, we list the $B(E2)$ between states within the ground and second bands of Ne isotopes, and of their corresponding hypernuclei. Due to the splitting of angular momentum into $J \pm 1/2$, each of the $B(E2)$ values of the core nucleus has two counterparts in hypernuclei, which are both listed. Unlike the shrinkage effect of Λ_s discovered previously on low-lying states [40,44], where the addition of one Λ_s enhances or reduces the $B(E2)$ in the ground or second band. This expansion and shrinkage effect are characterized by [67]

$$\Gamma_B = \frac{B\big(E2, J_i^+ \to J_f^+; {}^{A+1}_{\Lambda}\text{Ne}\big)}{B(E2, J_i^+ \to J_f^+; {}^{A}\text{Ne})}, \tag{18}$$

also listed in Table II.

In general, the $B(E2)$ are proportional to R_c^4 and to β^2 [40]. Both the shrinkage of the nuclear size indicated by R_c and the reduction of the quadrupole deformation $\bar{\beta}$, thus contribute to the overall reduction of $B(E2)$ [40,44]. As shown in Table II, Λ_s slightly reduces the $B(E2)$ within the ground band of $^{21-27,35}$Ne. The ratios Γ_B of $B(E2)$ between the states of hypernuclei to $B(E2)$ between the states of nuclei core are approximately 1 (highlighted in bold in Table II), while the ground bands of other isotopes are obviously influenced by Λ_s. It means that the deformations of the cores of $^{21-27,35}$Ne are relatively stable compared to those of other hyperisotopes, and an Λ_s is not enough to change it.

In addition, by comparing the $B(E2)$ within the ground band of the isotopes, it was found that the influence of Λ on $^{21}_{\Lambda}$Ne is greater than that on $^{23}_{\Lambda}$Ne and $^{25}_{\Lambda}$Ne. It should be explained from the following: Fig. 4 shows the potential energy surfaces of $^{21}_{\Lambda}$Ne, $^{23}_{\Lambda}$Ne, and $^{25}_{\Lambda}$Ne. We can clearly see the differences in the potential energy surfaces among these three isotopes: the depths of the valleys formed on both sides of the oblate and prolate shapes for $^{21}_{\Lambda}$Ne are about 1.5 MeV and 7 MeV, respectively; for $^{23}_{\Lambda}$Ne, they are about 2.5 MeV and 8 MeV, respectively; and for $^{25}_{\Lambda}$Ne, they are about 5 MeV and 4 MeV. Taking $^{21}_{\Lambda}$Ne as an example, according to the wave functions shown in Fig. 6, the reference states in the collective space contribute more to the ground band from the states within the two deeper valleys compared to states at other deformations, hence deeper valleys may lead to more stable collective states. Therefore, the ground band of $^{21}_{\Lambda}$Ne, which is mainly composed of reference states from the two valleys with depths of about 1.5 MeV and 7 MeV, is less stable compared to two others, making it more susceptible to changes induced by the addition of the Λ hyperon.

Further, the situation becomes more complicated for states in the second band of almost of Ne isotopes, where some $B(E2)$ increase or decrease. Such variations are also reflected in the $\bar{\beta}$ and rms radii. As shown in Table III, for some states, the average deformation $\bar{\beta}$ does not decrease due to the inclusion of Λ_s, but rather tends towards prolate deformation, while the radius decreases.

To investigate the impurity effect of Λ_s on low-lying states, the comparison of low-lying spectra of hypernuclei and nuclei are shown. In Fig. 5, the level structures of the second bands of ^{20}Ne and $^{21}_{\Lambda}$Ne, ^{22}Ne and $^{23}_{\Lambda}$Ne, and ^{24}Ne and $^{25}_{\Lambda}$Ne are given, and it is found that the addition of Λ_s appears

TABLE III. The excitation energies E, rms charge radii R_c, and average deformations $\bar{\beta}$ of the 0^+, 2^+, 4^+ states of ^{20,22,24,34}Ne and the $1/2^+$, $3/2^+$, $5/2^+$, $7/2^+$, $9/2^+$ states of $\Lambda(1s)$ $^{21,23,25,35}_{\Lambda}$Ne.

^{20}Ne				$^{21}_{\Lambda}$Ne			
J_i^π	E [MeV]	R_c [fm]	$\bar{\beta}$	J_i^π	E [MeV]	R_c [fm]	$\bar{\beta}$
$0^+_{\rm I}$	0.0	2.89	0.52	$1/2^+_{\rm I}$	−15.58	2.88	0.48
$2^+_{\rm I}$	1.36	2.89	0.62	$3(5)/2^+_{\rm I}$	−14.19 (−14.19)	2.88 (2.88)	0.56 (0.56)
$4^+_{\rm I}$	3.77	2.89	0.60	$7(9)/2^+_{\rm I}$	−11.83 (−11.90)	2.88 (2.87)	0.60 (0.58)
$6^+_{\rm I}$	7.43	2.86	0.57	$11(13)/2^+_{\rm I}$	−8.04 (−8.04)	2.86 (2.86)	0.56 (0.56)
$0^+_{\rm II}$	3.65	2.92	0.05	$1/2^+_{\rm II}$	−13.38	2.73	0.12
$2^+_{\rm II}$	5.69	2.92	0.18	$3(5)/2^+_{\rm II}$	−10.07 (−10.35)	2.81 (2.79)	0.27 (0.25)
$4^+_{\rm II}$	8.77	2.91	0.23	$7(9)/2^+_{\rm II}$	−6.41 (−6.45)	2.89 (2.88)	0.27 (0.23)
$6^+_{\rm II}$	14.36	2.88	0.16	$11(13)/2^+_{\rm II}$	−0.80 (−0.80)	2.93 (2.93)	0.26 (0.26)
^{22}Ne				$^{23}_{\Lambda}$Ne			
J_i^π	E [MeV]	R_c [fm]	$\bar{\beta}$	J_i^π	E [MeV]	R_c [fm]	$\bar{\beta}$
$0^+_{\rm I}$	0.0	2.96	0.50	$1/2^+_{\rm I}$	−16.33	2.94	0.47
$2^+_{\rm I}$	1.35	2.96	0.58	$3(5)/2^+_{\rm I}$	−14.93 (−14.93)	2.94 (2.94)	0.56 (0.56)
$4^+_{\rm I}$	3.97	2.95	0.59	$7(9)/2^+_{\rm I}$	−12.26 (−12.26)	2.93 (2.93)	0.57 (0.57)
$6^+_{\rm I}$	8.09	2.94	0.58	$11(13)/2^+_{\rm I}$	−8.16 (−8.16)	2.93 (2.92)	0.56 (0.56)
$0^+_{\rm II}$	3.74	2.85	0.18	$1/2^+_{\rm II}$	−12.94	2.81	0.11
$2^+_{\rm II}$	5.34	2.87	0.35	$3(5)/2^+_{\rm II}$	−10.62 (−11.17)	2.83 (2.84)	0.31 (0.34)
$4^+_{\rm II}$	7.88	2.94	0.40	$7(9)/2^+_{\rm II}$	−7.63 (−7.63)	2.88 (2.88)	0.32 (0.32)
$6^+_{\rm II}$	12.99	2.99	0.36	$11(13)/2^+_{\rm II}$	−2.18 (−2.18)	2.94 (2.94)	0.29 (0.29)
^{24}Ne				$^{25}_{\Lambda}$Ne			
J_i^π	E [MeV]	R_c[fm]	$\bar{\beta}$	J_i^π	E [MeV]	R_c[fm]	$\bar{\beta}$
$0^+_{\rm I}$	0.0	2.97	−0.03	$1/2^+_{\rm I}$	−17.10	2.95	−0.02
$2^+_{\rm I}$	2.49	2.97	−0.09	$3(5)/2^+_{\rm I}$	−14.54 (−14.52)	2.95 (2.95)	−0.08 (−0.08)
$4^+_{\rm I}$	6.38	2.97	−0.03	$7(9)/2^+_{\rm I}$	−10.44 (−10.49)	2.95 (2.95)	0.03 (0.03)
$6^+_{\rm I}$	12.35	2.97	0.16	$11(13)/2^+_{\rm I}$	−4.44 (−4.44)	2.95 (2.95)	0.15 (0.15)
$0^+_{\rm II}$	3.81	2.93	−0.09	$1/2^+_{\rm II}$	−13.28	2.92	−0.05
$2^+_{\rm II}$	6.13	3.01	0.33	$3(5)/2^+_{\rm II}$	−10.72 (−10.74)	3.00 (2.99)	0.34 (0.31)
$4^+_{\rm II}$	9.77	3.05	0.54	$7(9)/2^+_{\rm II}$	−6.70 (−6.81)	3.03 (3.03)	0.54 (0.50)
$6^+_{\rm II}$	14.33	3.15	0.77	$11(13)/2^+_{\rm II}$	−1.73 (−1.73)	3.21 (3.21)	0.96 (0.96)
^{34}Ne				$^{35}_{\Lambda}$Ne			
J_i^π	E [MeV]	R_c[fm]	$\bar{\beta}$	J_i^π	E [MeV]	R_c[fm]	$\bar{\beta}$
$0^+_{\rm I}$	0.0	3.42	0.41	$1/2^+_{\rm I}$	−18.62	3.40	0.40
$2^+_{\rm I}$	0.71	3.42	0.45	$3(5)/2^+_{\rm I}$	−17.89 (−17.89)	3.40 (3.40)	0.44 (0.44)
$4^+_{\rm I}$	2.06	3.41	0.45	$7(9)/2^+_{\rm I}$	−16.52 (−16.53)	3.40 (3.40)	0.45 (0.44)
$6^+_{\rm I}$	4.33	3.40	0.45	$11(13)/2^+_{\rm I}$	−14.38 (−14.38)	3.38 (3.38)	0.44 (0.44)
$0^+_{\rm II}$	5.49	3.35	0.02	$1/2^+_{\rm II}$	−13.59	3.33	0.06
$2^+_{\rm II}$	6.54	3.35	0.06	$3(5)/2^+_{\rm II}$	−12.23 (−12.34)	3.35 (3.34)	0.02 (0.03)
$4^+_{\rm II}$	8.81	3.36	0.14	$7(9)/2^+_{\rm II}$	−9.81 (−10.16)	3.37 (3.37)	0.18 (0.22)
$6^+_{\rm II}$	11.81	3.50	0.38	$11(13)/2^+_{\rm II}$	−6.98 (−7.07)	3.40 (3.39)	0.27 (0.25)

to affect the excitation modes of these bands. As shown in Fig. 5, this phenomenon is particularly evident in ^{20}Ne and $^{21}_{\Lambda}$Ne, and is also reflected in ^{22}Ne and $^{23}_{\Lambda}$Ne, ^{24}Ne and $^{25}_{\Lambda}$Ne, where structures resembling β vibration transition to vibration modes with equal energy gaps. This can be seen from the wave functions of ^{20}Ne and $^{21}_{\Lambda}$Ne given in the lower four subplots in Fig. 6, where the addition of Λ_s reduces the phase oscillation amplitude of the collective wave functions of states in the second band of ^{20}Ne.

In Fig. 5, the level structures of the second bands of ^{20}Ne and $^{21}_{\Lambda}$Ne, ^{22}Ne and $^{23}_{\Lambda}$Ne, and ^{24}Ne and $^{25}_{\Lambda}$Ne are given, and it is found that the addition of Λ_s appears to affect the excitation modes of these bands. As shown in Fig. 5, this phenomenon is particularly evident in ^{20}Ne and $^{21}_{\Lambda}$Ne, and is also reflected in ^{22}Ne and $^{23}_{\Lambda}$Ne, ^{24}Ne and $^{25}_{\Lambda}$Ne, where structures resembling β vibration transition to vibration modes with equal energy gaps. This can be seen from the wave functions of ^{20}Ne and $^{21}_{\Lambda}$Ne given in the lower four subplots in Fig. 6, where the

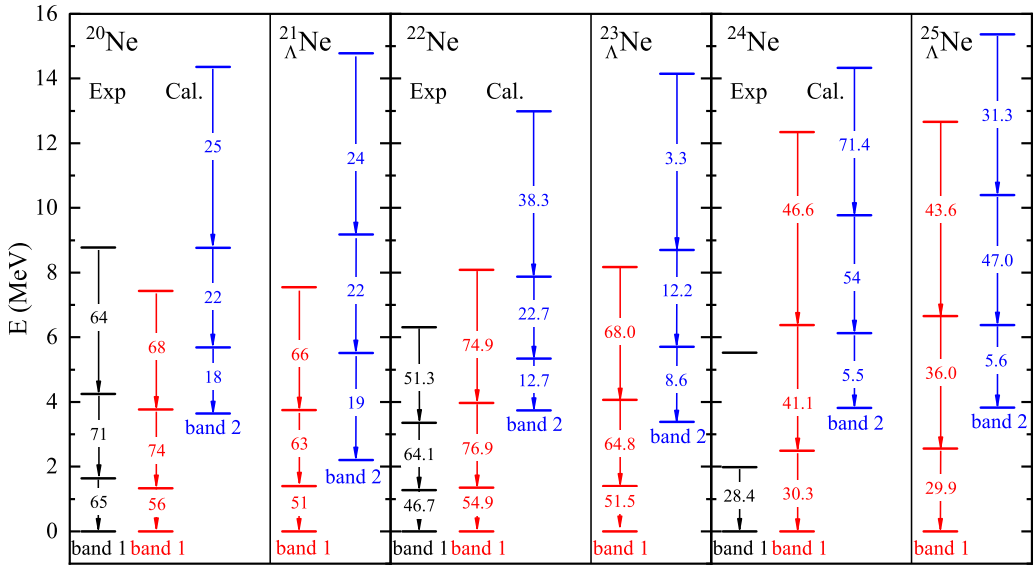

FIG. 5. Same as Fig. 2 but for comparison of hypernuclei and nuclei.

addition of Λ_s reduces the phase oscillation amplitude of the collective wave functions of states in the second band of ^{20}Ne.

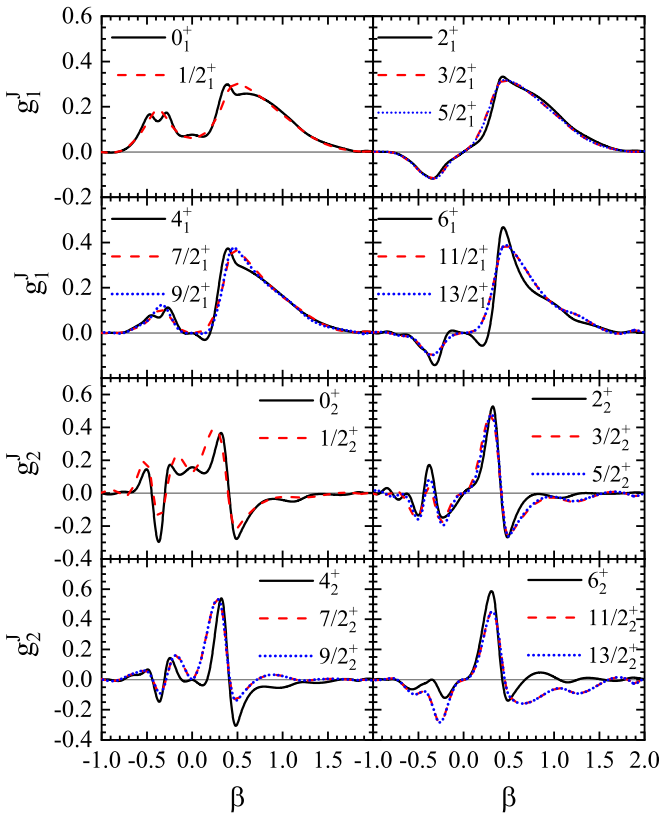

FIG. 6. Collective wave functions g^J_α for the low-lying states with $J = 0, 2, 4$, and 6 for ^{20}Ne and $J = 1/2, 3/2, 5/2, 7/9, 11/2, 13/2$ for $^{21}_{\Lambda}$Ne as a function of the deformation of the mean-field states from which they are constructed.

IV. SUMMARY

In summary, based on the results of the beyond mean field SHF approach, the shape coexistence of Ne isotopes is discussed at the mean field level and the beyond mean filed level, respectively. Then we studied the impurity effect of Λ on the low-lying spectra of these nuclei. The results of the mean field indicate that there is shape coexistence in the two isotopes ^{24}Ne and ^{28}Ne, due to the presence of two minima on the potential energy surface with similar energy but completely different shapes. The AMP provides additional shape coexistence nuclei: ^{26}Ne and ^{30}Ne. The results of GCM indicate that the ground states of ^{24}Ne, ^{26}Ne, and ^{28}Ne are not truly spherical, but are a mixture of prolate and oblate configurations. However, there is a phenomenon of strong mixing of different shapes within one physical state instead of coexistence of several physical states based on differently shaped configurations. The results of GCM indicate that shape coexistence is difficult to form in Ne isotopes.

In addition, well established rotational bands based on deformed ground states and β vibrational bands, whose collective wave functions exhibit positive and negative phase oscillations with similar structures to rotational bands, were found in the isotopes $^{20-24,34}$Ne.

Finally, we investigated the impurity effect of the s-state Λ on the band structure of Ne isotopes with coexisting shapes. We found that the s-state Λ has a shrinkage effect on the states in the ground band, similar to its effect on the ground state in the mean field. However, more dramatic is the influence of the Λ_s on the second band, which is quite unusual, as it seems to change the excitation mode of this band. The addition of the Λ_s results in an equidistant orientation within the band, shifting it from a β vibration band to a vibration band limit.

ACKNOWLEDGMENT

This work was supported by the National Natural Science Foundation of China under Grants No. 12175071, No. 12205103, and No. 11905165.

[1] P. E. Garrett, T. R. Rodríguez, A. D. Varela, K. L. Green, J. Bangay, A. Finlay, R. A. E. Austin, G. C. Ball, D. S. Bandyopadhyay, V. Bildstein *et al.*, Phys. Rev. Lett. **123**, 142502 (2019).

[2] S. Aberg, H. Flocard, and W. Nazarewicz, Annu. Rev. Nucl. Part. Sci. **40**, 439 (1990).

[3] P. E. Garrett, M. Zielińska, and E. Clément, Prog. Part. Nucl. Phys. **124**, 103931 (2022).

[4] K. Heyde and J. L. Wood, Rev. Mod. Phys. **83**, 1467 (2011).

[5] K. Heyde, P. Van Isacker, M. Waroquier, J. Wood, and R. Meyer, Phys. Rep. **102**, 291 (1983).

[6] J. Bonn, G. Huber, H.-J. Kluge, L. Kugler, and E. Otten, Phys. Lett. B **38**, 308 (1972).

[7] J. Bron, W. Hesselink, A. Van Poelgeest, J. Zalmstra, M. Uitzinger, H. Verheul, K. Heyde, M. Waroquier, H. Vincx, and P. Van Isacker, Nucl. Phys. A **318**, 335 (1979).

[8] E. Cheifetz, R. C. Jared, S. G. Thompson, and J. B. Wilhelmy, Phys. Rev. Lett. **25**, 38 (1970).

[9] P. Federman and S. Pittel, Phys. Lett. B **69**, 385 (1977).

[10] P. Federman and S. Pittel, Phys. Rev. C **20**, 820 (1979).

[11] U. Hager, A. Jokinen, V.-V. Elomaa, T. Eronen, J. Hakala, A. Kankainen, S. Rahaman, J. Rissanen, I. Moore, S. Rinta-Antila *et al.*, Nucl. Phys. A **793**, 20 (2007).

[12] J. H. Hamilton, A. V. Ramayya, W. T. Pinkston, R. M. Ronningen, G. Garcia-Bermudez, H. K. Carter, R. L. Robinson, H. J. Kim, and R. O. Sayer, Phys. Rev. Lett. **32**, 239 (1974).

[13] E. Caurier, G. Martínez-Pinedo, F. Nowacki, A. Poves, and A. P. Zuker, Rev. Mod. Phys. **77**, 427 (2005).

[14] T. Otsuka, M. Honma, T. Mizusaki, N. Shimizu, and Y. Utsuno, Prog. Part. Nucl. Phys. **47**, 319 (2001).

[15] K. Nomura, T. Otsuka, and P. V. Isacker, J. Phys. G: Nucl. Part. Phys. **43**, 024008 (2016).

[16] M. Bender, P.-H. Heenen, and P.-G. Reinhard, Rev. Mod. Phys. **75**, 121 (2003).

[17] L. M. Robledo, T. R. Rodríguez, and R. R. Rodríguez-Guzmán, J. Phys. G: Nucl. Part. Phys. **46**, 013001 (2019).

[18] T. Niki, D. Vretenar, and P. Ring, Prog. Part. Nucl. Phys. **66**, 519 (2011).

[19] H. Sagawa, X. R. Zhou, X. Z. Zhang, and T. Suzuki, Phys. Rev. C **70**, 054316 (2004).

[20] A. Li, E. Hiyama, X.-R. Zhou, and H. Sagawa, Phys. Rev. C **87**, 014333 (2013).

[21] R. Rodríguez-Guzmán, J. Egido, and L. Robledo, Eur. Phys. J. A **17**, 37 (2003).

[22] F. Nemoto, Y. Yamamoto, H. Horiuchi, Y. Suzuki, and K. Ikeda, Prog. Theor. Phys. **54**, 104 (1975).

[23] Y. Kanada-En'yo and H. Horiuchi, Prog. Theor. Phys. **93**, 115 (1995).

[24] M. Kimura, Phys. Rev. C **69**, 044319 (2004).

[25] Y. Taniguchi, M. Kimura, and H. Horiuchi, Prog. Theor. Phys. **112**, 475 (2004).

[26] H. Ohta, K. Yabana, and T. Nakatsukasa, Phys. Rev. C **70**, 014301 (2004).

[27] B. Zhou, Z. Ren, C. Xu, Y. Funaki, T. Yamada, A. Tohsaki, H. Horiuchi, P. Schuck, and G. Röpke, Phys. Rev. C **86**, 014301 (2012).

[28] E. Zhou, J. Yao, Z. Li, J. Meng, and P. Ring, Phys. Lett. B **753**, 227 (2016).

[29] P. Marević, J.-P. Ebran, E. Khan, T. Nikšić, and D. Vretenar, Phys. Rev. C **97**, 024334 (2018).

[30] F. Mercier, A. Bjelčić, T. Nikšić, J.-P. Ebran, E. Khan, and D. Vretenar, Phys. Rev. C **103**, 024303 (2021).

[31] A. Feliciello and T. Nagae, Rep. Prog. Phys. **78**, 096301 (2015).

[32] A. Gal, E. V. Hungerford, and D. J. Millener, Rev. Mod. Phys. **88**, 035004 (2016).

[33] H.-J. Schulze and E. Hiyama, Phys. Rev. C **90**, 047301 (2014).

[34] H.-T. Xue, Q. B. Chen, X.-R. Zhou, Y. Y. Cheng, and H. J. Schulze, Phys. Rev. C **106**, 044306 (2022).

[35] H.-T. Xue, Y.-F. Chen, Q. B. Chen, Y. A. Luo, H.-J. Schulze, and X.-R. Zhou, Phys. Rev. C **107**, 044317 (2023).

[36] Y.-F. Chen, X.-R. Zhou, Q. Chen, and Y.-Y. Cheng, Eur. Phys. J. A **58**, 21 (2022).

[37] J. Guo, C. F. Chen, X.-R. Zhou, Q. B. Chen, and H.-J. Schulze, Phys. Rev. C **105**, 034322 (2022).

[38] Y.-X. Liu, C. F. Chen, Q. B. Chen, H.-T. Xue, H.-J. Schulze, and X.-R. Zhou, Phys. Rev. C **108**, 064312 (2023).

[39] X. Li, C. F. Chen, X.-R. Zhou, and Z. Ren, Phys. Rev. C **109**, 064301 (2024).

[40] J.-W. Cui, X.-R. Zhou, L.-X. Guo, and H.-J. Schulze, Phys. Rev. C **95**, 024323 (2017).

[41] J.-W. Cui, R. Wang, and X.-R. Zhou, Chin. Phys. C **46**, 074109 (2022).

[42] H. Mei, K. Hagino, J. M. Yao, and T. Motoba, Phys. Rev. C **91**, 064305 (2015).

[43] H. Xia, X. Wu, H. Mei, and J. Yao, Sci. China: Phys., Mech. Astron. **62**, 42011 (2019).

[44] H.-T. Xue, Q. B. Chen, J.-W. Cui, C.-F. Chen, H.-J. Schulze, and X.-R. Zhou, Phys. Rev. C **109**, 024324 (2024).

[45] T. Motoba, H. Band, and K. Ikeda, Prog. Theor. Phys. **70**, 189 (1983).

[46] E. Hiyama, M. Kamimura, K. Miyazaki, and T. Motoba, Phys. Rev. C **59**, 2351 (1999).

[47] E. Hiyama, M. Kamimura, T. Motoba, T. Yamada, and Y. Yamamoto, Prog. Theor. Phys. **97**, 881 (1997).

[48] J. Yao, Z. Li, K. Hagino, M. Win, Y. Zhang, and J. Meng, Nucl. Phys. A **868–869**, 12 (2011).

[49] K. Hagino, J. Yao, F. Minato, Z. Li, and M. Thi Win, Nucl. Phys. A **914**, 151 (2013), XI International Conference on Hypernuclear and Strange Particle Physics (HYP2012).

[50] D. Vretenar, W. Pöschl, G. A. Lalazissis, and P. Ring, Phys. Rev. C **57**, R1060 (1998).

[51] X.-R. Zhou, A. Polls, H.-J. Schulze, and I. Vidaña, Phys. Rev. C **78**, 054306 (2008).

[52] H. Lü, J. Meng, S. Zhang, and S.-G. Zhou, Eur. Phys. J. A **17**, 19 (2003).

[53] E. Hiyama, M. Kamimura, T. Motoba, T. Yamada, and Y. Yamamoto, Phys. Rev. C **53**, 2075 (1996).

[54] H. Xia, X. Wu, H. Mei, and J. Yao, Sci. China: Phys., Mech. Astron. **66**, 252011 (2023).

[55] C. Chen, Q.-K. Sun, Y.-X. Li, and T.-T. Sun, Sci. China: Phys., Mech. Astron. **64**, 282011 (2021).

[56] M. Bender, K. Rutz, P. G. Reinhard, and J. A. Maruhn, Eur. Phys. J. A **8**, 59 (2000).

[57] P. Ring and P. Schuck, *The Nuclear Many Body Problem* (Springer, Verlag, Berlin, 1980).

[58] P. Bonche, J. Dobaczewski, H. Flocard, P.-H. Heenen, and J. Meyer, Nucl. Phys. A **510**, 466 (1990).

[59] M. Bender, P. Bonche, and P.-H. Heenen, Phys. Rev. C **74**, 024312 (2006).

[60] J. Dobaczewski *et al.*, Comput. Phys. Commun. **180**, 2361 (2009).
[61] T. Sumi, K. Minomo, S. Tagami, M. Kimura, T. Matsumoto, K. Ogata, Y. R. Shimizu, and M. Yahiro, Phys. Rev. C **85**, 064613 (2012).
[62] National Nuclear Data Center, https://www.nndc.bnl.gov/nudat3/.
[63] S. Hilaire and M. Girod, Eur. Phys. J. A **33**, 237 (2007).
[64] HFB results based on the Gogny force, https://www-phynu.cea.fr/science_en_ligne/carte_potentiels_microscopiques/carte_potentiel_nucleaire_eng.htm.
[65] A. Obertelli, S. Péru, J. P. Delaroche, A. Gillibert, M. Girod, and H. Goutte, Phys. Rev. C **71**, 024304 (2005).
[66] R. Rodríguez-Guzmán, J. Egido, and L. Robledo, Nucl. Phys. A **709**, 201 (2002).
[67] J.-W. Cui, X.-R. Zhou, and H.-J. Schulze, Phys. Rev. C **91**, 054306 (2015).